Journal of Materials Chemistry A

ROYAL SOCIETY OF CHEMISTRY

PAPER

View Article Online
View Journal | View Issue

Cite this: *J. Mater. Chem. A*, 2022, **10**, 19925

Vacancy assisted growth of copper tantalum sulfide nanocrystals†

Anamul Haque, [ab] Soheil Ershadrad, [c] Trupthi Devaiah Chonamada, [ab] Dipankar Saha, [de] Biplab Sanyal *[c] and Pralay K. Santra *[a]

Cu-based ternary chalcogenides have received significant interest as an alternative to conventional photovoltaic materials. $CuInS_2$ and $CuInSe_2$ are the most studied copper-based ternary chalcogenides for photovoltaics. Recently, copper tantalum sulfide ($CuTaS_3$) has been proposed as a potential light absorber for photovoltaics. The synthesis conditions and growth mechanism of ternary systems control the final composition and crystal structure. However, such studies have not been explored for copper tantalum sulfides. Here, we studied the formation and growth mechanism of Cu_3TaS_4 nanocrystals (NCs) primarily using X-ray diffraction, transmission electron microscopy, and density functional theory (DFT) calculations. The reactions proceed *via* the formation of cubic $Cu_{2-x}S$ NCs due to soft Lewis acid – soft Lewis base interaction. The $Cu_{2-x}S$ have Cu vacancies, which can be controlled by the relative concentration of the Cu precursor. Ta incorporation occurs in the $Cu_{2-x}S$ NCs at Cu vacancy sites, followed by the diffusion of Ta by replacing Cu into the lattice. Low packing of atoms in Cu_3TaS_4 provides suitable diffusion channels for Ta and Cu atoms. The diffusion barriers of Ta atoms outweigh that of Cu atoms, implying a reaction rate controlled by Ta diffusion. Thus by varying the relative Cu precursor concentration, the concentration of Cu-vacancies in $Cu_{2-x}S$ can be tuned, which controls the growth rate of Cu_3TaS_4. Understanding of the growth mechanism obtained in this paper will significantly contribute to the rational synthesis of various Cu-based ternary chalcogenides that is not possible by direct synthesis and hence will have an impact on potential applications in photovoltaics and photocatalysis.

Received 4th April 2022
Accepted 1st June 2022

DOI: 10.1039/d2ta02714c

rsc.li/materials-a

[a]*Centre for Nano and Soft Matter Sciences (CeNS), Bengaluru, 562162, India. E-mail: psantra@cens.res.in*

[b]*Manipal Academy of Higher Education (MAHE), Manipal, 576104, India*

[c]*Department of Physics and Astronomy, Materials Theory, Uppsala University, Box 516, SE-751 20, Uppsala, Sweden. E-mail: biplab.sanyal@physics.uu.se*

[d]*School of Chemical and Process Engineering, University of Leeds & CMAC, Leeds, LS29JT, UK*

[e]*Research Complex at Harwell (RCaH), Rutherford Appleton Laboratory, Harwell, Didcot, Oxon, OX11 0FA, UK*

† Electronic supplementary information (ESI) available. See https://doi.org/10.1039/d2ta02714c

Dr Pralay Santra joined the Centre for Nano and Soft Matter Sciences (CeNS) in November 2016 as a Scientist D. He did his undergraduate from St. Xavier's College, Kolkata, in 2003 with a major in Chemistry. Pralay then joined the Indian Institute of Science for the Integrated PhD program. He moved to the University of Notre Dame in 2011 to start his postdoctoral research. Later in 2013, he joined the Department of Chemical Engineering at Stanford University for another postdoctoral research. He was also at Uppsala University as Carl Trygger's postdoctoral fellow from 2015–2016. His research interests focus on fundamental understandings of various aspects of nanomaterials, growing sub-nanometer thick interfaces by atomic layer deposition and their applications. He and his team use multiple synchrotron-based experiments to probe the underlying properties of these materials. Dr Santra is rigorously involved in public outreach programs to an audience of high school and undergraduate students. He loves to travel and hike.

Introduction

Cadmium and lead-based chalcogenide nanocrystals (NCs) have gained interest in the photovoltaics (PV) community as emerging candidates for large-area, low-cost, and high-efficiency PV devices.[1–5] However, the usage of heavy metal ions limits the practical applicability of these materials.[6] Binary and ternary copper chalcogenide NCs have emerged as an alternative for heavy metal chalcogenides since these NCs can be directly synthesized with controlled sizes, shapes, crystal structures, and stoichiometries. As a result, they provide good control over the optoelectronic properties and serve as a template for ternary chalcogenides.[7–13] Additionally, relatively low cost and low toxicity of $Cu_{2-x}S$ and Cu-based ternary chalcogenides make them attractive candidates for PV as well as in photocatalysis.

Among the Cu-based ternary chalcogenides, $CuInS_2$ and $CuInSe_2$ are most studied as light absorbers in thin-film solar cells for over three decades.[14–17] Compared to the bulk, the NCs of these ternary chalcogenides have the added advantages of tuning electronic properties by controlling the size and can be deposited on various substrates by low-cost solution-based deposition.[18] These ternary chalcogenides NCs are synthesized in a one-pot synthesis – however, the reactivity of the two cationic precursors has to be balanced which is achieved by tuning the appropriate precursor, passivating ligand, and reaction temperature.[9,19–23] In a one-pot synthesis, both the cationic and anionic precursors are added together. Cu^+ is a soft Lewis acid ($\eta = 6.28$ eV) and the other cationic species *e.g.*, In^{3+}, Ga^{3+}, having a higher oxidation state, are generally hard Lewis acid.[20,24] A variety of sulfur precursors have been used in these reactions, which vary from soft Lewis base (*e.g.*, alkanethiols,[19] 1-dodecanethiol[25]) to hard Lewis base (*e.g.*, thiourea[26–28]).

In many cases, the binary nanocrystals are first synthesized followed by subsequent cation exchange to form desired ternary or heterostructured NCs. Owing to the low charge and high mobility of Cu^+, the post-synthetic cation exchange is feasible in $Cu_{2-x}S$ to produce multiple heterostructures – $Cu_{2-x}S$–MnS,[29] $Cu_{2-x}S$–ZnS,[30–35] $Cu_{2-x}S$–CdS,[36] $Cu_{2-x}S$–PbS,[37] $Cu_{2-x}S$–In_2S_3.[38,39] The final heterostructure depends on various parameters such as cationic radius, the initial crystal structure, and the reactivity of the facets of the crystal through which the cation exchange occurs, *etc.* Chen *et al.*, have reported the different crystal structures of CdS when the cation exchange is performed on djurleite $Cu_{1.94}S$ (wurtzite CdS) and covellite CuS (hollow cubic CdS).[40] Manna *et al.* have observed that the InP nucleate at the corners of hexagonal $Cu_{2-x}P$ before propagating inward towards the center for a complete conversion of $Cu_{2-x}S$ to InP NCs.[41] In both homovalent and aliovalent cation exchange processes, the nanoscale Kirkendall effect caused hollow ternary chalcogenides.[26,42–45] Sapra *et al.*, have developed $MoSe_2$–Cu_2S nanoheterostructures, where the Cu_2S islands grow vertically on top of the defect site present on the $MoSe_2$ surface.[46] Donega *et al.*, have indeed reported the $CuInS_2$ NCs and $Cu_{2-x}S$-$CuInS_2$ heterostructured NCs by partial indium cation exchange into $Cu_{2-x}S$ NCs.[47,48] Steimle *et al.*, have demonstrated a multi-step sequential cation exchange of $Cu_{1.8}S$ nanorod to form multicomponent axially segmented heteronanorods having eight segments, six different elements, and 11 interfaces.[49]

In 2017, Heo *et al.* theoretically identified $CuTaS_3$ as a strong light absorber that exhibits metal *d* and sulfur *p* character near the band edges.[50] As this material has intermetal d^0–d^{10} transitions, it can exhibit a strong onset coupled with high absorption. Based on spectroscopic limited maximum efficiency for PV calculations, they predicted the theoretical power conversion efficiency to be 28% for a 300 nm thick absorber of $CuTaS_3$, which is higher than the $CuInSe_2$ of the same thickness. The Cu-based ternary chalcogenides often exhibit multiple phases, and it is important to study the growth of these nanocrystals. The synthesis of Cu–Ta–S ternary chalcogenides NCs was not attempted earlier. Due to its potential applications, it is important to synthesize the Cu–Ta–S ternary chalcogenide, particularly in NCs that helps in solution processed device fabrication. Overall, the understanding of the growth mechanism of such NCs systems is also required for rational synthesis of Cu-based ternary chalcogenides.

Here we report the hot injection synthesis of copper tantalum sulfide NCs. We carried out the reactions under three different reaction conditions – Cu rich, Ta rich, and equimolar concentration of Cu and Ta. Experimentally, we probed the formation and growth mechanism by X-ray diffraction and transmission electron microscopy (TEM). Under all three reaction conditions, cubic Cu_3TaS_4 NCs were formed. Rietveld analysis and UV-Vis absorption studies show the formation of $Cu_{2-x}S$ NCs at the beginning of the reaction followed by Ta incorporation into $Cu_{2-x}S$ NCs, converting them to Cu_3TaS_4 NCs. These results were further substantiated with high-resolution transmission electron microscopic (HRTEM) images. We used density functional theory (DFT) to calculate the energetics and predict the diffusion model for Ta incorporation into $Cu_{2-x}S$ NCs to form Cu_3TaS_4 NCs.

Experimental section

Chemicals

Copper(I) chloride (CuCl, 99.995%, Sigma-Aldrich), tantalum(V) chloride ($TaCl_5$, 99.999%, Sigma-Aldrich), carbon disulfide (CS_2, 99.5%, Central Drug House (P) Ltd) oleylamine (OLA, 70%, Sigma-Aldrich), and *n*-hexane (95%, Spectrochem), methanol (>98%, Spectrochem) were used as received.

Synthesis of Cu–Ta–S nanocrystals

In a 50 mL three-neck round bottom flask, CuCl and $TaCl_5$ were taken in 14.76 mL (44.8 mmol) of OLA. The reaction mixture were heated at 120 °C for 1 hour under vacuum. The total cation precursor (Cu + Ta) was kept constant at 5.84 mmol, whereas the relative concentrations of Cu and Ta precursors were varied. The individual quantities are mentioned in Table S1 in the ESI.† The reaction temperature was increased to 290 °C under a nitrogen atmosphere to completely dissolve the precursor salts and held the reaction mixture was kept for 1 hour to ensure

the complete dissolution of the precursors. Before the sulfur precursor injection, the reaction temperature was raised to 300 °C. 1.35 mL of CS_2 was swiftly injected into the reaction flask. Periodically aliquots were collected from the reaction mixture to probe the growth mechanism of the NCs. The schematic diagram of the synthesis procedure is shown in Fig. S1.†

The collected aliquots were cooled to room temperature before diluting with hexane. The diluted reaction mixture was centrifuged at 3000 rpm for 3 minutes to get the precipitate of the nanoparticles, which were washed two times by dispersing in 2 mL hexane and reprecipitating with 6 mL of methanol. The washed precipitate was finally dispersed in hexane for further characterization.

Characterization

A PerkinElmer, Lambda-45 UV-vis spectrometer was used to record the UV-visible absorption spectra. Powder X-ray diffraction (PXRD) of the NCs were carried out on drop cast thin-films on glass substrates using a Rigaku Smart Lab diffractometer equipped with parallel beam optics and Cu Kα radiation (40 kV, 30 mA) with a grazing angle of 2°. Transmission electron microscopy studies were carried out using the TALOS F200S G2 microscope at 200 kV.

Rietveld refinement

Rietveld refinements[51] were carried out using *FullProf Suite*.[52] Refined instrumental parameters were zero point displacement and background parameters. Refined structural parameters for all phases were scale factor, unit cell parameters and peak profile using Thompson–Cox–Hastings pseudo-Voigt (TCHpV) profile parameters.[52] Instrumental resolution was taken into account by refining TCHpV profile parameters for the Si standard and included them in an instrumental resolution file (*.irf) implemented in the refinements.

Computational methods

First-principles calculations based on density functional theory (DFT) were performed using the Vienna *Ab initio* Simulation Package (VASP).[53,54] For these calculations, projector-augmented wave potentials[55] and a plane-wave basis set with an energy cut-off of 500 eV was employed. The exchange-correlation potential was approximated by the generalized gradient approximation (GGA) with Perdew, Burke, and Ernzerhof (PBE) functional.[56] For Brillouin zone integration of Cu_2S and Cu_3TaS_4, a 9 × 9 × 9 *k*-point grid in the Monkhorst–Pack scheme[57] was used. To simulate the vacancies, a supercell of 2 × 2 × 2 was built and the vacancies were created in this structure at random positions. The equilibrium configuration of atoms and lattice constants was determined by minimizing the total energy of the system using the conjugate gradient method until force components on each atom were reached below 0.01 eV $Å^{-1}$. Saddle points and minimum energy diffusion paths between two stable states were found through climbing image Nudged Elastic Band (NEB) calculations, using VTST tool,[58] where five intermediate images along the diffusion path were considered and a spring force of −5 eV $Å^{-2}$ was set between them. Vacancy formation energies were calculated using the following expression,

$$E_f = E_{Cu_{2-x}S} - E_{Cu_2S} + E_{Fcc-Cu}$$

where, E_f is the formation energy, and the terms on the right hand side are the total energy of the crystal with vacancy, the total energy of the stoichiometric crystal, and the energy of one Cu atom in bulk face centered cubic (FCC) form, respectively. Formation energies of stoichiometric crystals were calculated with respect to the bulk form of each constituting element.

Surface calculations were performed on a 2 × 2 supercell of a thin film with three unit cell thickness (expanded parallel to surface), where a vacuum of 20 Å was added along the *c*-axis to avoid interaction between periodic images. Since rearrangement of atoms only occurs near the surface, the position of atoms in the lowermost layers in the unit cell along the *c*-axis was fixed during geometry optimization to maintain the bulk properties. The surface energy of different crystalline facets was calculated based on the following expression,

$$\sigma = \frac{E_{surf} - E_{bulk} \times N}{2A}$$

where, σ is the surface energy, E_{surf} is the total energy of the slab's supercell, E_{bulk} is the energy of bulk per atom, N is the number of atoms in the slab, and A is the surface area of the facet supercell.

Results and discussion

Cu–Ta–S is known to exist in two different crystal structures – the orthorhombic phase having a composition of $CuTaS_3$ and the cubic phase of Cu_3TaS_4.[50,59] The synthesis of the Cu–Ta–S NCs was carried out by the standard hot injection method with an excess amount of the sulfur precursor (molar ratio ∼1 : 8). The details of the synthesis procedure are mentioned in the experimental section. The powder X-ray diffraction (PXRD) pattern of the washed NCs synthesized with a 1 : 1 ratio of Cu : Ta is shown in Fig. 1a along with the two standard diffraction patterns: orthorhombic $CuTaS_3$ (space group: *Pnma*) and cubic Cu_3TaS_4 (space group: $P\bar{4}3m$). The nanocrystals formed in the cubic phase, instead of the intended orthorhombic phase which has the cation (Cu : Ta) ratio of 1 : 1. Separate syntheses having Cu-rich (Cu : Ta = 3 : 1) and Ta-rich (Cu : Ta = 1 : 3) precursor concentrations were also carried out, however, both the conditions yielded NCs in the cubic Cu_3TaS_4 phase only (Fig. S2 in the ESI†). In agreement with experimental results, *ab initio* calculations also indicate that the formation of Cu_3TaS_4 instead of $CuTaS_3$ NCs is more favoured from an energetic point of view. In fact, calculation of the formation energy per formula unit (f.u) of the cubic Cu_3TaS_4 and orthorhombic $CuTaS_3$ phases (shown in Table S2†) revealed that the cubic phase has a formation energy of −4.99 eV $f.u^{-1}$ (−0.62 eV per atom) which is quite lower than the orthorhombic phase (−2.49 eV $f.u^{-1}$ equivalent to −0.50 eV per atom). We believe that this energetic privilege of Cu_3TaS_4, added to its better

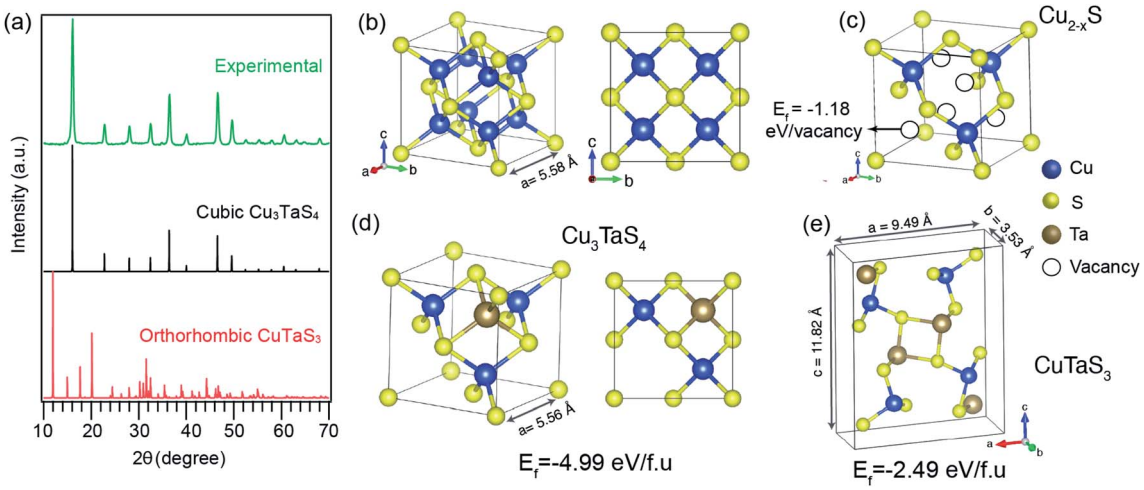

Fig. 1 (a) PXRD pattern of the synthesized nanocrystals (green line) (after 30 min reaction) compared with standard orthorhombic phase $CuTaS_3$ (red line) and cubic phase Cu_3TaS_4 (black line). Ball and stick model of (b) Cu_2S, (c) $Cu_{2-x}S$, (d) cubic Cu_3TaS_4, and (e) orthorhombic $CuTaS_3$, where blue, yellow, and brown balls represent Cu, S, and Ta atoms, respectively. E_f denotes the formation energies of vacancies in (c), and bulk crystal in (d) and (e).

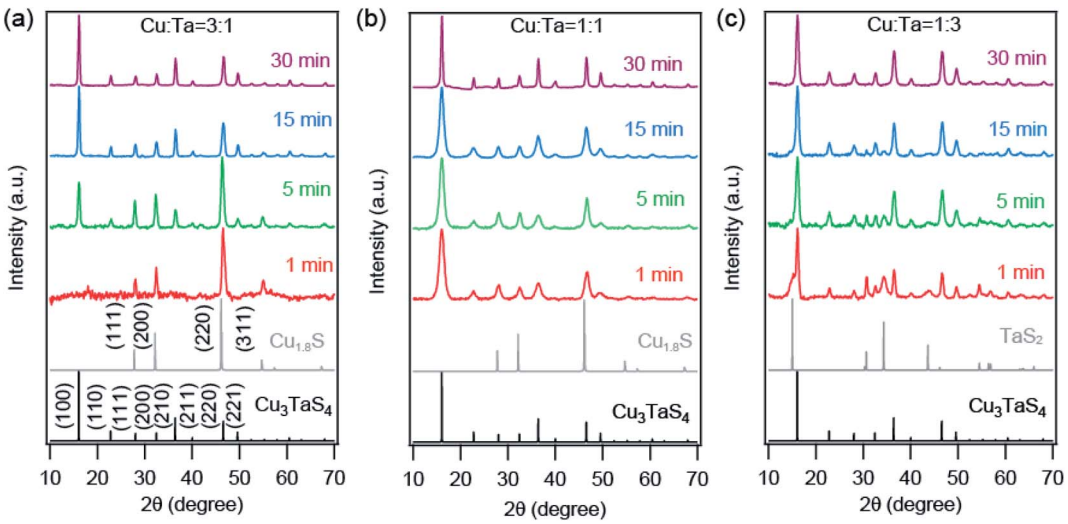

Fig. 2 XRD patterns of synthesized Cu–Ta–S NCs for (a) Cu : Ta = 3 : 1, (b) Cu : Ta = 1 : 1, and (c) Cu : Ta = 1 : 3 reactions, collected at different reaction times. The standard cubic phase of Cu_3TaS_4 ($P\bar{4}3m$) and $Cu_{2-x}S$ ($Fm\bar{3}m$; $x = 0.2$) are shown by black and grey solid line.

structural compatibility with $Cu_{2-x}S$, drive the system to form Cu_3TaS_4 crystals, instead of $CuTaS_3$.

From a structural point of view, the transformation of $Cu_{2-x}S$ into Cu_3TaS_4 can be modelled *via* a diffusion-mediated mechanism. For this purpose, the structural configuration of cubic Cu_2S crystal is shown in Fig. 1b, where Cu atoms occupy tetrahedral sites, each of which is bonded to four S atoms, creating symmetrically equivalent Cu sites. By optimizing the given structure, the lattice parameter and the symmetry group were found to be $a = 5.58$ Å and $Fm\bar{3}m$, respectively. In Fig. 1c, the formation of vacancies in tetrahedral sites is schematically shown. We calculated the formation energy of vacancies for a $Cu_{1.8}S$, with a vacancy concentration of 9.37% to be −1.18 eV per vacancy, verifying the spontaneous formation of vacancies in Cu_2S. As the concentration of vacancies increases, around $x = 0.4$, another cubic phase of $Cu_{2-x}S$ becomes stable with a symmetry of $F\bar{4}3m$. To predict which of these phases is dominant in the process, we calculated the vacancy formation energy in $Cu_{1.6}S$ to be −0.5 eV per vacancy. In addition, we found that the formation energy of $Cu_{1.8}S$ is 20 meV per atom lower than that of $Cu_{1.6}S$ crystals, calculated with respect to bulk sulfur and FCC copper. Therefore, it can be inferred that in presence of sufficient Cu atoms, the formation of $Cu_{1.8}S$ crystal is energetically more favorable compared to $Cu_{1.6}S$. Considering $Cu_{1.8}S$ as the initial phase of the reaction, the formation of Cu_3TaS_4 crystals can be justified based on the structural similarities between the two crystals. For ease of comparison, the crystal structure of Cu_3TaS_4 and $CuTaS_3$ are shown in Fig. 1d

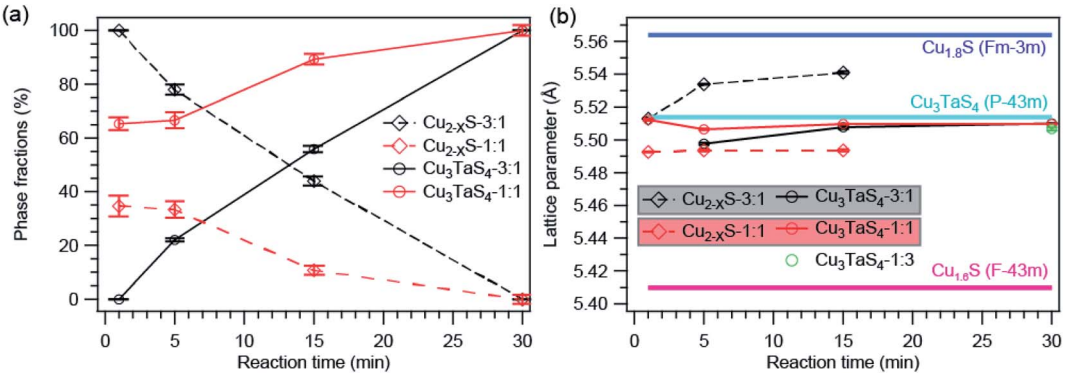

Fig. 3 Analysis from Rietveld refinement profile. (a) Phase fractions of $Cu_{2-X}S$ and Cu_3TaS_4 as a function of reaction time. (b) The calculated lattice parameters of $Cu_{2-X}S$ and Cu_3TaS_4 compared with standard lattice parameters of $Cu_{1.8}S$, $Cu_{1.6}S$, and Cu_3TaS_4.

Table 1 The relative phase fractions of $Cu_{2-x}S$ and Cu_3TaS_4 at different reaction times for Cu : Ta = 3 : 1 and 1 : 1 reaction

Cu : Ta = 3 : 1			Cu : Ta = 1 : 1		
	Phase fraction			Phase fraction	
Reaction time (min)	$Cu_{2-x}S$	Cu_3TaS_4	Reaction time (min)	$Cu_{2-x}S$	Cu_3TaS_4
1	100	0	1	34.6 ± 3.8	65.4 ± 2.4
5	78.0 ± 1.84	22.0 ± 0.6	5	33.4 ± 3.1	66.6 ± 3.0
15	44.0 ± 1.69	56.0 ± 1.2	15	10.7 ± 1.7	89.3 ± 2.0
30	0	100	30	0	100

and e, respectively. The lattice parameter and symmetry group of Cu_3TaS_4 were calculated to be $a = 5.56$ Å and $P\bar{4}3m$. One can note that, in contrast to $CuTaS_3$, the crystal structure of Cu_2S, $Cu_{2-x}S$, and Cu_3TaS_4 basically share the same skeleton except for a number of substitutions that take place between Cu, vacancy, and Ta atoms. Compatibility of the lattice parameters in Cu_2S (5.58 Å) and Cu_3TaS_4 (5.56 Å), combined with their overall similarity, suggest that after the spontaneous formation of vacancies in Cu_2S, Ta atoms diffuse into the $Cu_{2-x}S$ structure to create Cu_3TaS_4 crystals.

We further probed the growth mechanism of the ternary chalcogenide NCs by collecting the reaction aliquots at different times. The PXRD patterns of the precipitates of the reaction mixture for the Cu-rich (Cu : Ta = 3 : 1) reaction at different times are shown in Fig. 2a. The diffraction peaks of the precipitate collected at the early stage of the reaction match with the cubic $Cu_{2-x}S$ ($x = 0.2$). After five minutes of the reaction, new peaks appeared and those are identified to Cu_3TaS_4. The diffraction peaks of $Cu_{2-x}S$ overlaps with Cu_3TaS_4. With the progress of the reaction, the intensity of the $Cu_{2-x}S$ (220) peak decreases while Cu_3TaS_4 (100) peak intensity increases, implying that $Cu_{2-x}S$ NCs are converting to Cu_3TaS_4. Beyond 30 minutes of the reaction, the diffraction peak positions and the intensities do not vary and the pattern matches well with Cu_3TaS_4 suggesting the end product of the reaction is the cubic phase Cu_3TaS_4. For an equal amount of Cu and Ta (Cu : Ta = 1 : 1), Cu_3TaS_4 was already present at the early stage of the reaction, with probably some amount of $Cu_{2-x}S$ (Fig. 2b). Due to the overlapping peaks, the presence of both the phases could not be confirmed from these qualitative observations. However, at the end of the reaction, *i.e.*, 30 minutes, only the cubic Cu_3TaS_4 was observed. In the Ta-rich synthesis (Cu : Ta = 1 : 3), we observed a mixture of TaS_2 and Cu_3TaS_4 at the beginning of the reaction as shown in Fig. 2c. The PXRD pattern of TaS_2 (space group: $P\bar{3}m1$) is clearly distinct from the Cu_3TaS_4 or $Cu_{2-x}S$. In this case, the TaS_2 peaks disappear with time and only Cu_3TaS_4 NCs are present at the end of the reaction, suggesting that all TaS_2 are converted to Cu_3TaS_4 NCs. From these PXRD results, we conclude that the variation of precursor amount in the reaction plays a role during the growth of the NCs, but the final composition remains the same. In a Cu-rich reaction, cubic $Cu_{2-x}S$ forms at an early stage, which then converts to Cu_3TaS_4; whereas in a Ta-rich reaction, TaS_2 forms first and then converts to Cu_3TaS_4. The formation rate of Cu_3TaS_4 varies with the relative concentration of the Cu and Ta precursors.

We employed Rietveld refinement to quantify (a) the relative phase fraction, (b) lattice parameter, and (c) particles sizes of $Cu_{2-x}S$ and Cu_3TaS_4 in the reaction. The PXRD patterns along with the Rietveld refinement profiles for three different precursor concentrations are shown in Fig. S3.† The resulting phase fractions of $Cu_{2-x}S$ (dashed traces with open circles) and Cu_3TaS_4 (solid traces with filled circles) for reaction 3 : 1 (black traces) and 1 : 1 (red trace) are shown in Fig. 3a. For the Cu-rich reaction, the phase fraction of $Cu_{2-x}S$ is 100% at the beginning of the reaction, however, the relative phase fraction of $Cu_{2-x}S$

decreases rapidly, and consequently the amount of Cu_3TaS_4 increases (see Table 1). At the end of 30 minutes of the reaction, the phase fraction of Cu_3TaS_4 is found to be 100%. Unlike the Cu-rich reaction, the Cu : Ta = 1 : 1 has 65% as Cu_3TaS_4 and 35% of $Cu_{2-x}S$, clearly indicating the formation of Cu_3TaS_4 is faster in a Cu-deficient system. By the end of 15 minutes, the major product is Cu_3TaS_4 NCs with a relative phase fraction of 89%.

The lattice parameters of $Cu_{2-x}S$ and Cu_3TaS_4 as a function of the reaction time are shown in Fig. 3b (lattice parameters are mentioned in Table S3† and Rietveld refinement factors are mentioned in Table S4†). For comparison, the lattice parameter of standard $Cu_{1.8}S$ (ICSD file number: 41142) and cubic Cu_3TaS_4 (ICSD file number: 185524) are shown by the solid horizontal blue and cyan line. Lattice parameter of $Cu_{2-x}S$ (shown by the dashed line) increases as a function of time for both reactions. Earlier reports suggest that $Cu_{2-x}S$ with higher vacancies have relatively smaller lattice parameters.[60] The lattice parameter of standard $Cu_{2-x}S$ for $x = 0.4$ (ICSD file number: 628786) is shown by the horizontal purple line. Although both the $Cu_{1.6}S$ and $Cu_{1.8}S$ have cubic crystal structures, the lattice parameter of $Cu_{1.6}S$ is much smaller than $Cu_{1.8}S$. Indirectly, the increase in the lattice parameter indirectly suggests the Cu vacancies in $Cu_{2-x}S$ decrease with reaction time. Also, the lattice parameter of $Cu_{2-x}S$ at a given reaction time is higher for the Cu-rich reaction compared to the 1 : 1 reaction indicating fewer Cu vacancies in $Cu_{2-x}S$ for the Cu-rich reaction. At the same time, there was no significant change in Cu_3TaS_4.

In literature, it is well known that the Cu vacancies in $Cu_{2-x}S$ NCs exhibit a localized surface plasmon resonance (LSPR) peak in the NIR region.[61] We collected the absorption spectra for different reactions to understand how the LSPR, thus Cu-vacancies vary with reaction time. The absorption spectra of the NCs for three different precursor concentrations at different reaction times are shown in Fig. S4 in the ESI.† At the early stage of the reactions, a broad absorption peak appears at ~1100 nm, which is due to the LSPR of $Cu_{2-x}S$, which was noticed for the Cu-rich and 1 : 1 precursor ratio. The LSPR peak for the Cu-rich reaction was low in intensity and decreases with reaction time. The same LSPR peak for the 1 : 1 reaction has a much higher intensity at the beginning of the reaction and it red-shifts as well as the intensity of the peak decreases with the reaction time. We did not observe the typical LSPR peak for the Cu : Ta = 1 : 3 reaction. These results suggest that the Cu-rich reaction forms $Cu_{2-x}S$ with a fewer number of Cu-vacancies, whereas the vacancy increases significantly with a decrease in the Cu precursor in the reaction mixture. The increase of Cu vacancy in $Cu_{2-x}S$ for the lower Cu reaction supports the Rietveld refinement results. It is worthful to note that the reaction proceeds faster with increasing Cu vacancy in $Cu_{2-x}S$ system.

We also investigated the growth of these NCs through transmission electron microscopy (TEM). Representative TEM images are shown in Fig. 4 for all three precursor ratios.

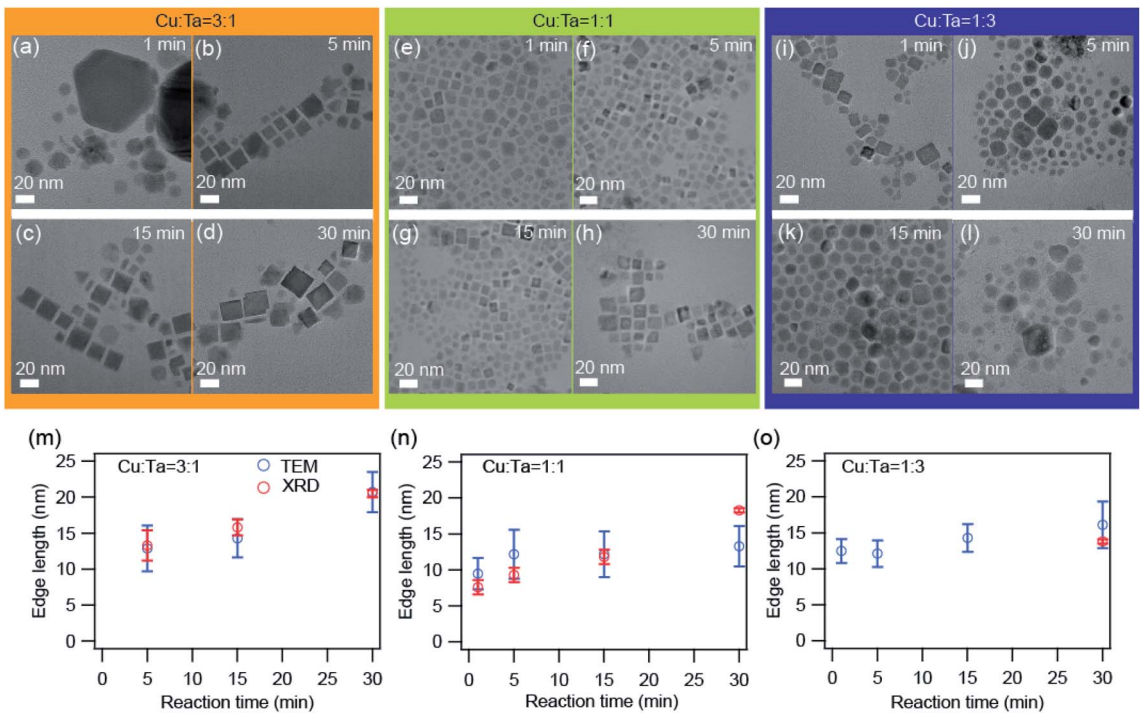

Fig. 4 TEM images of the synthesized NCs. (a–d) Cu : Ta = 3 : 1, (e–h) Cu : Ta = 1 : 1, and (i–l) Cu : Ta = 1 : 3 for different reaction times: 1 min, 5 min, 15 min, and 30 min. The scale bar is 20 nm. The average edge length as a function of reaction time for (m) Cu : Ta = 3 : 1, (n) Cu : Ta = 1 : 1, and (o) Cu : Ta = 1 : 3. The error bars indicate the size distribution. The average size calculated from TEM images are shown by blue solid circles and the size calculated from the XRD peaks after Rietveld refinement is shown by open black circles. The size distribution histograms are shown in Fig. S5.†

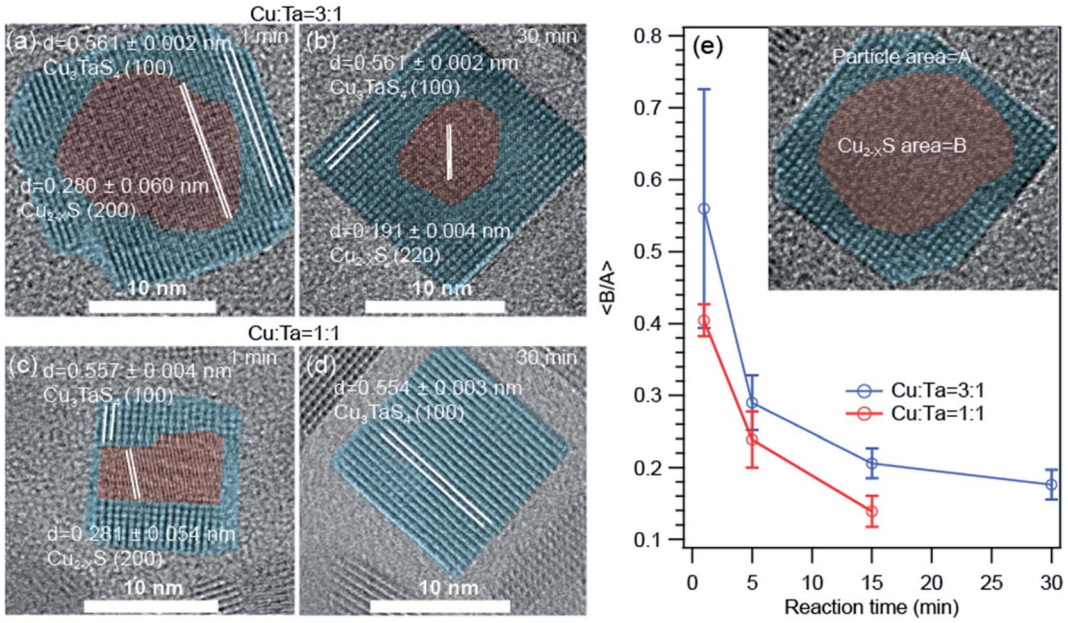

Fig. 5 High resolution transmission electron microscopy (HRTEM) images of the core–shell type $Cu_{2-x}S$ – Cu_3TaS_4 NCs. (a and b) NCs of 1 min, and 30 min reaction for Cu : Ta = 3 : 1. (c and d) NCs of 1 min, and 30 min reaction for Cu : Ta = 1 : 1. The HRTEM images for Cu; Ta = 1 : 3 reactions are shown in Fig. S6.† (e) The average of core to particle area ratio as a function of reaction time for Cu : Ta = 3 : 1 and Cu : Ta = 1 : 1. Inset figure is schematic presentation of the core–shell type $Cu_{1.8}S$ – Cu_3TaS_4 NCs.

Primarily the big particles (~90 nm) of $Cu_{2-x}S$ were present at the very beginning (~1 minute) for the Cu-rich reaction. With reaction time, these bigger particles transformed into smaller particles (~10 nm) having a square shape, and these can be identified as Cu_3TaS_4 NCs. The average particle size of Cu_3TaS_4 NCs increases from ~10 nm to ~20 nm with the reaction time, as shown in Fig. 4m. For Cu : Ta = 1 : 1, the square-shaped Cu_3TaS_4 NCs particles were present at the beginning of the reaction and there were no changes in the overall shape of the particles. For Ta-rich samples, we have the square-shaped particles, which become slightly irregular in shape with the progress of the reaction time. Both the average size and size distribution increase with the reaction. We compared the average size as measured from TEM with the crystallite sizes calculated from the Rietveld analysis of the diffraction pattern and both the sizes match well with each other, suggesting all the particles are highly crystalline – that could be due to the high-temperature synthesis.

The high-resolution transmission electron microscopic (HRTEM) images show some interesting information about the growth of these NCs. The representative images for Cu-rich and 1 : 1 ratio of Cu and Ta are shown in Fig. 5. We found that a core–shell heterostructure has formed at an early stage of the reaction. We highlighted the core with brown color and the shell with cyan color. The interplanar distances (0.28 nm and 0.19 nm) of the core region either matched with the (200) or (220) planes of $Cu_{1.8}S$. The interplanar distances (0.51 nm) of the shell region are larger than the core region and match with the (100) plane of Cu_3TaS_4. We observed this heterostructure only for the Cu-rich and Cu : Ta = 1 : 1 reaction. With reaction time, both the number of such heterostructured NCs goes down as well as the average size of the core $Cu_{2-x}S$ decreases. For the Ta-rich reaction, TaS_2 and Cu_3TaS_4 particles were separately present at the beginning of the reaction as shown in Fig. S6† and TaS_2 NCs were not observed at the later stage of the reaction.

As the area of the core and shell region in the TEM images represent the volume of the respective materials, we quantified the respective ratios of the core to shell region as a function of reaction time for Cu-rich and 1 : 1 ratio of Cu and Ta (Fig. 5e) to understand how the core–shell structure vanish with time. The core is indicated with an area of 'A' and the overall particle with an area of 'B' as shown in the inset. We find that the average core to shell area ratio decreases systematically with increasing reaction time. The rate of this change is higher for the 1 : 1 ratio of Cu and Ta compared to the Cu-rich reaction.

To bring better insight into the mechanism of Ta incorporation in $Cu_{2-x}S$ crystals, we computationally studied the formation energies and diffusion barriers of the low-index surfaces. We found that the probability of finding Ta atoms as interstitial (2.31 eV per defect) or substitution (3.73 eV per defect) defects is marginal, due to unfavourable formation energies. In contrast, it was found that vacancy sites are suitable settlements for Ta atoms. Accordingly, the formation energy of the first Ta atom, to occupy one out of six vacancies in a 2 × 2 × 2 supercell of $Cu_{1.8}S$, is −1.60 eV per Ta. Adding another Ta to this system changes the formation energy to $E_f = -0.24$ eV per Ta. After the number of Ta atoms passes a threshold (three in this case), the formation energy changes sign (with $E_f = 0.06$, 0.96 and 1.28 eV per Ta for third, fourth and fifth Ta atoms, respectively), a signal that the crystal has reached its capacity and cannot accept more Ta atoms. An interpretation can be that

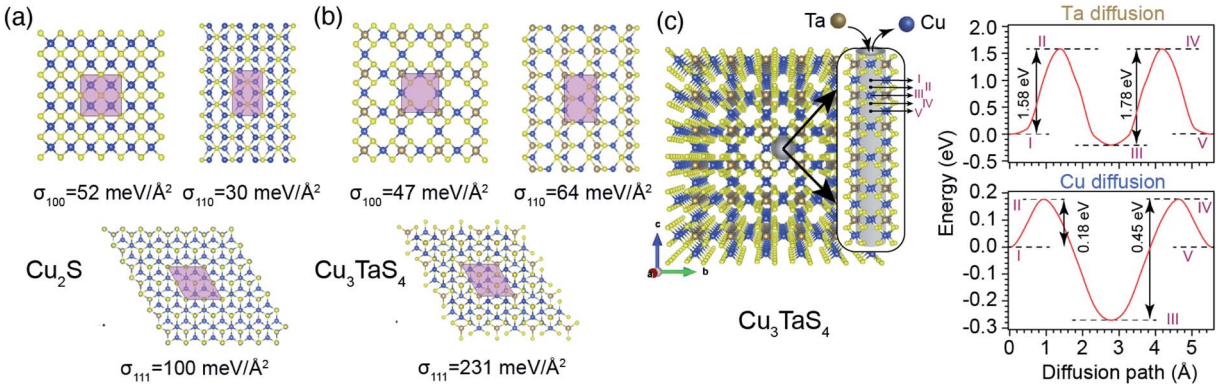

Fig. 6 Schematics of low index surfaces of (a) Cu_2S and (b) Cu_3TaS_4, from the top view, where light pink areas are 1×1 unit cells, and σ is the surface formation energy. (c). Left panel demonstrates diffusion channels perpendicular to {100} planes inside Cu_3TaS_4 bulk, where the cylindrical grey shadow, in the inset, schematically shows the Ta and Cu diffusion path. Right panels are the diffusion energy barriers for Ta and Cu along the diffusion channel, where the Roman numerals are used to link the crystal coordinates to their corresponding points along the diffusion path.

in addition to the inward diffusion of Ta, extra Cu atoms need to diffuse out from the region where Cu_3TaS_4 is going to be formed.

Based on these assumptions, we predict that the formation of experimentally observed core–shell structure is governed by a diffusion mediated mechanism, where the concentration gradient pushes Ta atoms to diffuse from the solution into the $Cu_{2-x}S$ structure, and extra Cu atoms need to move out to create a Cu depleted zone, required for the formation of Cu_3TaS_4. As a side effect of this collective movement, the vacancy sites in the path of the migrant Cu atoms get occupied, dwindling the vacancy concentration of the core $Cu_{2-x}S$ region, and increasing its lattice parameter (see Fig. 3b, and its discussion). Since the primary nucleation of Cu_3TaS_4 appears on facets, we studied energetics by calculating the surface energies of the low index planes in Cu_2S as shown in Fig. 6a. It can be seen that the most stable planes are the {110} family with a surface energy of 30 meV $Å^{-2}$. The {100} planes come in second place with 52 meV $Å^{-2}$, and {111} planes are the least energetically favourable ones with 100 meV $Å^{-2}$. Although these results suggest that Cu_2S NCs only expose their {110} surfaces, we believe that due to the deformation caused by vacancies at the high reaction temperature ($T = 300$ °C), the preferred surface of $Cu_{2-x}S$ can be a combination of these facets, as evident in Fig. 5. We further calculated the diffusion barrier of one Ta atom to get incorporated into each of these surfaces. To do this, the initial stage of Ta diffusion was considered to be 3 Å above the surface, and the final stage was Ta located in a vacant site. We found that along all paths, the diffusion barriers are relatively low, zero in the case of diffusion into {100} surface, 6 and 67 meV for {110} and {111} surfaces, respectively. The size of these energy barriers is small enough to be overcome by the thermal fluctuation of atoms at $T = 300$ °C. Thus, we predict that the nucleation and growth of Cu_3TaS_4 should start uniformly from all facets, leading to a semi-spherical core of $Cu_{2-x}S$, similar to what can be seen in Fig. 5. We also calculated the surface formation energy of Cu_3TaS_4 for low index cubic planes (see Fig. 6b). It was found that energetically, Cu_3TaS_4 crystals should prefer to expose their {100} surfaces more than the other ones as σ_{100} (47 meV $Å^{-2}$) < σ_{110} (64 meV $Å^{-2}$) < σ_{111} (231 meV $Å^{-2}$). Thus, as a rule of thumb, the clean cubic surfaces found in Fig. 5, can be attributed to the formation of {100} facets in Cu_3TaS_4 NCs. We further estimated the diffusion barrier of Ta inside the bulk of $Cu_{2-x}S$. In this tightly packed structure, Ta needs to overcome a large energy barrier of 5.63 eV to diffuse between two neighbouring vacant Cu sites. The magnitude of this energy barrier shows that the diffusion of Ta into the depth of $Cu_{2-x}S$ is a rare event, and $Cu_{2-x}S$ to Cu_3TaS_4 transformation takes place at the boundary of two phases, leading to the formation of a core–shell structure. After the initial formation of Cu_3TaS_4 on facets, Ta atoms need to diffuse through the bulk structure of Cu_3TaS_4 to reach Ta depleted inner zones. Meanwhile, to satisfy stoichiometric constraints, a portion of Cu atoms needs to diffuse out of the $Cu_{2-x}S$ core and along their way, they have to pass through Cu_3TaS_4 shell. Thus, we further studied the energy costs of Ta and Cu diffusion into bulk Cu_3TaS_4, where the results are shown in Fig. 6c. The low packing concentration of atoms in Cu_3TaS_4 provides suitable diffusion channels (parallel to ⟨100⟩ crystal edges) for Ta and Cu atoms as evident from Fig. 6c. We calculated the energy landscape along these diffusion paths, finding that Ta atoms have to overcome two periodic diffusion barriers of 1.58 and 1.78 eV, with a periodicity equivalent to that of Cu_3TaS_4 unit cell (5.56 Å). In a similar scenario, Cu atoms can escape the core region by overcoming two periodic diffusion barriers of 0.18 eV and 0.45 eV, while passing the Cu_3TaS_4 diffusion channels.

Combining all these pieces to create a collective picture, the formation of the core–shell structure can be explained. Firstly, Ta atoms diffuse into Cu vacancy sites readily available on the surface of $Cu_{2-x}S$ to form primary nucleation sites for growth of Cu_3TaS_4. The lower formation energy of Cu_3TaS_4 compared to $Cu_{2-x}S$ propels this structural transformation further, by causing an outward flow of Cu atoms through diffusion channels that naturally exist in Cu_3TaS_4 structure. Simultaneously,

the Ta concentration gradient creates a flow of Ta atoms in a direction opposite to that of Cu atoms, through the same diffusion channels. Since the diffusion barrier for Ta atoms are more than three times higher than that of Cu atoms (bigger size of Ta atoms is one contributing factor to this), the rate of reaction is controlled by Ta diffusion. As the core of NCs is not easily reachable for Ta atoms, NCs form a core–shell structure, where the size of inner core region shrinks by the passage of reaction time. The size of $Cu_{2-x}S$ parent crystals is one of the factors that determines the core to shell ratio during the reaction. In other words, bigger $Cu_{2-x}S$ crystals are more prone to keep the remnant core region even at the end of the reaction. Another contributing factor is the vacancy concentration in $Cu_{2-x}S$ crystals, to host the Ta atoms. A higher vacancy concentration will make Ta incorporation faster and also create a finer distribution of Cu_3TaS_4 nucleation sites. Since vacancy concentration depends on the relative precursor concentrations, we can tune this to control the reaction rate.

Conclusion

In this work, we synthesized cubic Cu_3TaS_4 NCs by hot injection synthesis. Due to the soft Lewis acid nature of Cu^+, it reacts with CS_2, a soft Lewis base to form cubic $Cu_{2-x}S$. Further, Ta gets incorporated into the $Cu_{2-x}S$ NCs at the Cu vacancy site followed by the diffusion through the lattice. A Cu-rich reaction produces a lesser amount of Cu vacancies and slower incorporation of Ta, whereas a Cu deficit or low concentration condition produces a larger concentration of Cu vacancies that helps in faster incorporation of Ta, thus the faster formation of Cu_3TaS_4 NCs. DFT calculations suggest that Ta prefers to occupy the Cu vacancies in $Cu_{2-x}S$, followed by Ta diffusion into the lattice. Simultaneously, an outward flow of Cu atoms maintains the stoichiometric constraints imposed by Cu_3TaS_4. The strength of the energy barrier for Ta diffusion is similar for {100}, {110} and {111} surfaces, which allows the nucleation growth of Cu_3TaS_4 uniformly through all facets as observed in HRTEM images. Higher energy barriers found along the Ta diffusion path compared to Cu atoms imply that the reaction is controlled by the sluggish Ta diffusion, which is the origin of the core–shell structure found in NCs. The insights provided here will help in developing the synthesis of other ternary chalcogenides – which are otherwise not possible by direct synthesis.

Author contributions

P. K. S. conceived the idea and supervised the experimental work and B. S. led the theoretical work. A. H. carried out the synthesis and characterization. T. D. C. assisted in TEM measurements and analysis. D. S. analyzed the powder XRD data (with A. H.). S. E. performed the DFT calculations (with B. S.). All authors discussed the results and contributed to writing the manuscript.

Conflicts of interest

There are no conflicts of interest to declare.

Acknowledgements

The authors acknowledge the Central Research Facilities, Centre for Nano and Soft Matter Sciences, Bengaluru. TEM Facility, funded by a TPF Nanomission, GoI project at the Centre is gratefully acknowledged. The authors also acknowledge the Department of Science and Technology, India, and SERB (CRG/2018/001698) for the financial support. A. H. acknowledges the student fellowship from the Centre. T. D. C acknowledges the Inspire Fellowship from the Department of Science and Technology (DST), India. The computations were enabled in project SNIC 2021/3-38 by resources provided by the Swedish National Infrastructure for Computing (SNIC) at NSC, PDC and HPC2N partially funded by the Swedish Research Council through grant agreement no. 2018-05973. B. S. also acknowledges allocation of supercomputing hours in PRACE DECI-17 project Q2Dtopomat. B. S. acknowledges financial support from the Swedish Research Links programme Grant (2017-05447) provided by Swedish Research Council.

References

1 H. Fu, *J. Mater. Chem. C*, 2018, **6**, 414–445.
2 J. Patel, F. Mighri, A. Ajji and T. K. Chaudhuri, *Nano Energy*, 2014, **5**, 36–51.
3 Y. Min, G. D. Moon, C. E. Kim, J.-H. Lee, H. Yang, A. Soon and U. Jeong, *J. Mater. Chem. C*, 2014, **2**, 6222–6248.
4 M. V. Kovalenko, *Nat. Nanotechnol.*, 2015, **10**, 994–997.
5 D. Wang, F. Yin, Z. Du, D. Han and J. Tang, *J. Mater. Chem. A*, 2019, **7**, 26205–26226.
6 H. Ron, *Environ. Health Perspect.*, 2006, **114**, 165–172.
7 A. C. Berends, M. J. J. Mangnus, C. Xia, F. T. Rabouw and C. de Mello Donega, *J. Phys. Chem. Lett.*, 2019, **10**, 1600–1616.
8 K. E. Knowles, K. H. Hartstein, T. B. Kilburn, A. Marchioro, H. D. Nelson, P. J. Whitham and D. R. Gamelin, *Chem. Rev.*, 2016, **116**, 10820–10851.
9 A. D. P. Leach and J. E. Macdonald, *J. Phys. Chem. Lett.*, 2016, **7**, 572–583.
10 W. van der Stam, A. C. Berends and C. de Mello Donega, *ChemPhysChem*, 2016, **17**, 559–581.
11 D. Moodelly, P. Kowalik, P. Bujak, A. Pron and P. Reiss, *J. Mater. Chem. C*, 2019, **7**, 11665–11709.
12 D. Aldakov, A. Lefrançois and P. Reiss, *J. Mater. Chem. C*, 2013, **1**, 3756–3776.
13 L. De Trizio and L. Manna, *Chem. Rev.*, 2016, **116**, 10852–10887.
14 S. Ishizuka, J. Nishinaga, K. Beppu, T. Maeda, F. Aoyagi, T. Wada, A. Yamada, J. Chantana, T. Nishimura, T. Minemoto, M. M. Islam, T. Sakurai and N. Terada, *Phys. Chem. Chem. Phys.*, 2022, **24**, 1262–1285.
15 A. Ennaoui, M. Bär, J. Klaer, T. Kropp, R. Sáez-Araoz and M. C. Lux-Steiner, *Prog. Photovoltaics*, 2006, **14**, 499–511.
16 R. Klenk, J. Klaer, R. Scheer, M. C. Lux-Steiner, I. Luck, N. Meyer and U. Rühle, *Thin Solid Films*, 2005, **480–481**, 509–514.
17 R. Scheer, R. Klenk, J. Klaer and I. Luck, *Sol. Energy*, 2004, **77**, 777–784.

18 C. Coughlan, M. Ibáñez, O. Dobrozhan, A. Singh, A. Cabot and K. M. Ryan, *Chem. Rev.*, 2017, **117**, 5865–6109.
19 R. Xie, M. Rutherford and X. Peng, *J. Am. Chem. Soc.*, 2009, **131**, 5691–5697.
20 J. Kolny-Olesiak and H. Weller, *ACS Appl. Mater. Interfaces*, 2013, **5**, 12221–12237.
21 H. Zhong, S. S. Lo, T. Mirkovic, Y. Li, Y. Ding, Y. Li and G. D. Scholes, *ACS Nano*, 2010, **4**, 5253–5262.
22 H. Zhong, Y. Zhou, M. Ye, Y. He, J. Ye, C. He, C. Yang and Y. Li, *Chem. Mater.*, 2008, **20**, 6434–6443.
23 J. J. Nairn, P. J. Shapiro, B. Twamley, T. Pounds, R. von Wandruszka, T. R. Fletcher, M. Williams, C. Wang and M. G. Norton, *Nano Lett.*, 2006, **6**, 1218–1223.
24 S. O. M. Hinterding, A. C. Berends, M. Kurttepeli, M.-E. Moret, J. D. Meeldijk, S. Bals, W. van der Stam and C. de Mello Donega, *ACS Nano*, 2019, **13**, 12880–12893.
25 L. Li, A. Pandey, D. J. Werder, B. P. Khanal, J. M. Pietryga and V. I. Klimov, *J. Am. Chem. Soc.*, 2011, **133**, 1176–1179.
26 H.-J. Yang, C.-Y. Chen, F.-W. Yuan and H.-Y. Tuan, *J. Phys. Chem. C*, 2013, **117**, 21955–21964.
27 C. Yu, J. C. Yu, H. Wen and C. Zhang, *Mater. Lett.*, 2009, **63**, 1984–1986.
28 Y. Vahidshad, M. N. Tahir, A. I. zad, S. M. Mirkazemi, R. Ghazemzadeh and W. Tremel, *J. Mater. Chem. C*, 2015, **3**, 889–898.
29 J. Zhou, F. Huang, J. Xu and Y. Wang, *CrystEngComm*, 2013, **15**, 4217–4220.
30 L. Yi, A. Tang, M. Niu, W. Han, Y. Hou and M. Gao, *CrystEngComm*, 2010, **12**, 4124–4130.
31 S.-K. Han, M. Gong, H.-B. Yao, Z.-M. Wang and S.-H. Yu, *Angew. Chem., Int. Ed.*, 2012, **51**, 6365–6368.
32 F. Huang, X. Wang, J. Xu, D. Chen and Y. Wang, *J. Mater. Chem.*, 2012, **22**, 22614–22618.
33 H. Ye, A. Tang, L. Huang, Y. Wang, C. Yang, Y. Hou, H. Peng, F. Zhang and F. Teng, *Langmuir*, 2013, **29**, 8728–8735.
34 D.-H. Ha, A. H. Caldwell, M. J. Ward, S. Honrao, K. Mathew, R. Hovden, M. K. A. Koker, D. A. Muller, R. G. Hennig and R. D. Robinson, *Nano Lett.*, 2014, **14**, 7090–7099.
35 C. Xia, A. Pedrazo-Tardajos, D. Wang, J. D. Meeldijk, H. C. Gerritsen, S. Bals and C. de Mello Donega, *Chem. Mater.*, 2021, **33**, 102–116.
36 M. D. Regulacio, C. Ye, S. H. Lim, M. Bosman, L. Polavarapu, W. L. Koh, J. Zhang, Q.-H. Xu and M. Y. Han, *J. Am. Chem. Soc.*, 2011, **133**, 2052–2055.
37 T. T. Zhuang, F. J. Fan, M. Gong and S.-H. Yu, *Chem. Commun.*, 2012, **48**, 9762–9764.
38 S. H. Choi, E. G. Kim and T. Hyeon, *J. Am. Chem. Soc.*, 2006, **128**, 2520–2521.
39 W. Han, L. Yi, N. Zhao, A. Tang, M. Gao and Z. Tang, *J. Am. Chem. Soc.*, 2008, **130**, 13152–13161.
40 L. Chen, Z. Kong, H. Tao, H. Hu, J. Gao and G. Li, *Nanoscale*, 2022, **14**, 3907–3916.
41 L. De Trizio, R. Gaspari, G. Bertoni, I. Kriegel, L. Moretti, F. Scotognella, L. Maserati, Y. Zhang, G. C. Messina, M. Prato, S. Marras, A. Cavalli and L. Manna, *Chem. Mater.*, 2015, **27**, 1120–1128.
42 G. Xiao, Y. Zeng, Y. Jiang, J. Ning, W. Zheng, B. Liu, X. Chen, G. Zou and B. Zou, *Small*, 2013, **9**, 793–799.
43 H. Cao, X. Qian, C. Wang, X. Ma, J. Yin and Z. Zhu, *J. Am. Chem. Soc.*, 2005, **127**, 16024–16025.
44 G. Chen, M. Niu, L. Cui, F. Bao, L. Zhou and Y. Wang, *J. Phys. Chem. C*, 2009, **113**, 7522–7525.
45 L. Mu, F. Wang, B. Sadtler, R. A. Loomis and W. E. Buhro, *ACS Nano*, 2015, **9**, 7419–7428.
46 M. S. Hassan, S. Bera, D. Gupta, S. K. Ray and S. Sapra, *ACS Appl. Mater. Interfaces*, 2019, **11**, 4074–4083.
47 C. Xia, C. H. M. van Oversteeg, V. C. L. Bogaards, T. H. M. Spanjersberg, N. L. Visser, A. C. Berends, J. D. Meeldijk, P. E. de Jongh and C. de Mello Donega, *ACS Nano*, 2021, **15**, 9987–9999.
48 W. van der Stam, A. C. Berends, F. T. Rabouw, T. Willhammar, X. Ke, J. D. Meeldijk, S. Bals and C. de Mello Donega, *Chem. Mater.*, 2015, **27**, 621–628.
49 B. C. Steimle, J. L. Fenton and R. E. Schaak, *Science*, 2020, **367**, 418–424.
50 J. Heo, L. Yu, E. Altschul, B. E. Waters, J. F. Wager, A. Zunger and D. A. Keszler, *Chem. Mater.*, 2017, **29**, 2594–2598.
51 H. M. Rietveld, *J. Appl. Crystallogr.*, 1969, **2**, 65–71.
52 J. Rodríguez-Carvajal, *Phys. B*, 1993, **192**, 55–69.
53 G. Kresse and D. Joubert, *Phys. Rev. B*, 1999, **59**, 1758–1775.
54 G. Kresse and J. Hafner, *J. Phys.: Condens. Matter*, 1994, **6**, 8245–8257.
55 P. E. Blöchl, *Phys. Rev. B*, 1994, **50**, 17953–17979.
56 J. P. Perdew, K. Burke and M. Ernzerhof, *Phys. Rev. Lett.*, 1996, **77**, 3865–3868.
57 H. J. Monkhorst and J. D. Pack, *Phys. Rev. B*, 1976, **13**, 5188–5192.
58 G. Henkelman, B. P. Uberuaga and H. Jónsson, *J. Chem. Phys.*, 2000, **113**, 9901–9904.
59 A. B. Kehoe, D. O. Scanlon and G. W. Watson, *J. Mater. Chem. C*, 2015, **3**, 12236–12244.
60 A. A. Ivanov, I. V Tarasova, V. T. Bublik, R. K. Akchurin, I. V Shchetinin, N. Y. Tabachkova, D. A. Pshenay-Severin and V. B. Osvenskii, *Phys. Solid State*, 2018, **60**, 2295–2299.
61 Y. Xie, A. Riedinger, M. Prato, A. Casu, A. Genovese, P. Guardia, S. Sottini, C. Sangregorio, K. Miszta, S. Ghosh, T. Pellegrino and L. Manna, *J. Am. Chem. Soc.*, 2013, **135**, 17630–17637.

